


 Cite this: *RSC Adv.*, 2022, **12**, 30522

# Outstanding fluoride removal from aqueous solution by a La-based adsorbent†

 Weisen Yang,<sup>a</sup> Fengshuo Shi,<sup>a</sup> Wenlong Jiang,<sup>a</sup> Yuhuang Chen,<sup>a</sup> Kaiyin Zhang,<sup>c</sup> Shaoju Jian,<sup>id</sup>\*<sup>a</sup> Shaohua Jiang,<sup>id</sup><sup>ab</sup> Chunmei Zhang<sup>\*d</sup> and Jiapeng Hu<sup>\*a</sup>

A La-based adsorbent was prepared with  $\text{La}(\text{NO}_3)_3 \cdot 6\text{H}_2\text{O}$ , 2-methylimidazole and DMF via amide-hydrolysis and used for fluoride decontamination from aqueous water. The obtained adsorbent was lanthanum methanoate ( $\text{La}(\text{COOH})_3$ ). The effects of pH value, initial  $\text{F}^-$  concentration and interfering ions on defluoridation properties of as-prepared  $\text{La}(\text{COOH})_3$  were assessed through batch adsorption tests. The adsorption kinetics, isotherm models and thermodynamics were employed to verify the order, nature and feasibility of  $\text{La}(\text{COOH})_3$  towards fluoride removal. The results imply that  $\text{La}(\text{COOH})_3$  is preferable for defluoridation over a wide pH range of 2 to 9 without interference. Simultaneously, the defluoridation process of  $\text{La}(\text{HCOO})_3$  accords to the pseudo-second order model and Langmuir isotherm, revealing chemical adsorption is the main control step. The maximum fluoride capture capacities of  $\text{La}(\text{COOH})_3$  at 30, 40 and 50 °C are 245.02, 260.40 and 268.99  $\text{mg g}^{-1}$ , respectively. The mechanism for defluoridation by  $\text{La}(\text{COOH})_3$  was revealed by PXRD and XPS. To summarize, the as-synthesized La based adsorbent could serve as a promising adsorbent for defluoridation from complex fluoride-rich water.

 Received 6th October 2022  
 Accepted 20th October 2022

DOI: 10.1039/d2ra06284d

[rsc.li/rsc-advances](https://rsc.li/rsc-advances)

## 1. Introduction

The fluoride pollution in aquatic ecosystems has drawn global concern in recent years. Excessive intake of fluoride from water leads to thyroid disease, osteoporosis, skeletal and dental fluorosis, and even brain damage.<sup>1</sup> Groundwater with high fluoride is exposed in more than 25 countries such as India, American, Pakistan, Africa, Sri Lanka, Mexico, China and so on.<sup>2,3</sup> Accordingly, exploring an efficient and feasible fluoride remediation technology is imperative. Up to now, various remediation options for defluoridation such as anion exchange,<sup>4</sup> membrane technology,<sup>5</sup> adsorption,<sup>6</sup> precipitation-coagulation,<sup>7</sup> reverse osmosis (RO),<sup>8</sup> and electro dialysis<sup>9,10</sup> were conventionally established for fluoride retention. Among these water purification techniques, adsorption technology has been

indicated to be an eye-catching and economical option owing to its comprehensive benefits of simplicity of design, operational flexibility, inexpensive expenditure, and high efficiency. A great variety of adsorbents like nano sized metal-oxide adsorbents,<sup>11</sup> carbon-based adsorbents,<sup>12</sup> glass fibers,<sup>13</sup> montmorillonite,<sup>2</sup> Mxenes,<sup>14,15</sup> polymers,<sup>16–18</sup> clay,<sup>19,20</sup> and metal-organic frameworks (MOFs)<sup>21–24</sup> have been designed to recover fluoride ions and metal ions in water. However, most traditional defluoridation adsorbents have the limitations of low removal efficiency, are highly pH-dependent over a narrow pH range or have poor selectivity.

Currently, adsorbents based on rare-earth metal element have been recognized as effective adsorbent materials. Zr MOFs based on  $\text{ZrCl}_4$  and tetrafluoroterephthalic acid exhibited good defluoridation performance over a wide pH range of 3 to 10 with the maximum uptake of 204.08  $\text{mg g}^{-1}$  computed by Langmuir model.<sup>25</sup> Various La-based materials have been widely utilized for remediation of phosphate, metal ions, arsenic and fluoride because of the strong affinity and high selectivity of rare earth metal lanthanum (La), the biocompatible, the low cost, and environmentally friendly.<sup>26–28</sup> The La-MOF@50%PANI, which was fabricated with terephthalic acid (1,4-BDC) ligand through a one-pot technique possessed superior removal efficiency toward  $\text{Pb}^{2+}$  with maximum capture uptake of 185.19  $\text{mg g}^{-1}$ .<sup>29</sup> Yin *et al.* explored five La-MOFs *viz.* La-BTC, La-BDC, La-BPDC, La-PMA, and La-BHTA for immobilization of fluoride, the maximum uptake of fluoride reached 105.2, 171.7, 125.9, 158.9 and 145.5  $\text{mg g}^{-1}$  at 25 °C, respectively.<sup>3</sup> Fe–Mg–La tri-metal

<sup>a</sup>Fujian Key Laboratory of Eco-Industrial Green Technology, College of Ecology and Resources Engineering, Wuyi University, Wuyishan 354300, China. E-mail: [jianshaoju@126.com](mailto:jianshaoju@126.com); [wuyuwqhjp@163.com](mailto:wuyuwqhjp@163.com)

<sup>b</sup>Jiangsu Co-Innovation Center of Efficient Processing and Utilization of Forest Resources, International Innovation Center for Forest Chemicals and Materials, College of Materials Science and Engineering, Nanjing Forestry University, Nanjing 210037, China

<sup>c</sup>College of Mechanical and Electrical Engineering, Wuyi University, Wuyishan 354300, China

<sup>d</sup>Institute of Materials Science and Devices, School of Materials Science and Engineering, Suzhou University of Science and Technology, Suzhou 215009, China. E-mail: [cmzhang@usts.edu.cn](mailto:cmzhang@usts.edu.cn)

† Electronic supplementary information (ESI) available. See DOI: <https://doi.org/10.1039/d2ra06284d>



nanocomposite<sup>30</sup> prepared by co-precipitation without calcination exhibit efficient defluorination performance with maximum capacity of 47.2 mg g<sup>-1</sup>. Prabhu S M *et al.*<sup>31</sup> developed La(HCOO)<sub>3</sub> through an acid catalyst amide-hydrolysis mechanism using lanthanum nitrate hexahydrate, benzoic acid (BA) and DMF as materials. The maximum adsorption of AsO<sub>4</sub><sup>3-</sup> by La(COOH)<sub>3</sub> was found to be 2.623 mmol g<sup>-1</sup>. Until now, La(COOH)<sub>3</sub> prepared with La(NO<sub>3</sub>)<sub>3</sub>·6H<sub>2</sub>O, 2-methylimidazole and DMF *via* basic amide-hydrolysis mechanism and used as an adsorbent for defluorination has never been reported.

Herein, La-based adsorbent (lanthanum methanoate) was fabricated *via* amide-hydrolysis mechanism for abating excess F<sup>-</sup> from aqueous solution. Characterization of the as-prepared adsorbent was thoroughly evaluated by SEM, PXRD and XPS. The defluorination property of La(COOH)<sub>3</sub> was quantified in detail. To elucidate the mechanism of fluoride decontamination by La(COOH)<sub>3</sub>, the kinetics models and adsorption isotherms were systematically studied *via* adsorption.

## 2. Experimental

### 2.1. Materials

La(NO<sub>3</sub>)<sub>3</sub>·6H<sub>2</sub>O (99.9%), *N,N*-dimethylformamide (DMF, 99.5%), NaF (99%), 2-methylimidazole (98%), NaOH (≥98%), NaCl (99.5%), HCl (37%), CH<sub>3</sub>OH (99.9%), and other used chemicals were obtained from Aladdin Reagents Co., Ltd and used directly.

### 2.2. Synthesis of La-based adsorbent

1.300 g of La(NO<sub>3</sub>)<sub>3</sub>·6H<sub>2</sub>O and 0.825 g of 2-methylimidazole were dissolved thoroughly in 40 mL of DMF under stirring for 10 min, respectively. Then the above solutions were mixed under vigorous stirring for 30 min, and reacted at 150 °C for 2 h in a 150 mL solvothermal autoclave. Subsequently, in order to eliminate the unreacted agents from pores of lanthanum methanoate, the precipitation was washed with reaction solvent and methanol several times and dried at 80 °C. The preparation scheme of La-based adsorbent was displayed in Scheme 1.

### 2.3. Adsorption tests

The 100 mg L<sup>-1</sup> F<sup>-</sup> standard stock solution was prepared by pouring an appropriate amount of NaF into 1 L deionized (DI) water. For batch defluorination experiments, 0.01 g lanthanum methanoate was immersed in to 50 mL of F<sup>-</sup> solution at 30 °C for 12 h in triplicate. Adsorption kinetics examinations were performed with 1 L of F<sup>-</sup> solution (10 and 20 mg L<sup>-1</sup> calculated by the mass of fluoride anions). To investigate the adsorption isotherms, the defluorination experiments were conducted by varying the initial F<sup>-</sup> concentration (10–80 mg L<sup>-1</sup>) at 30, 40 and

50 °C, respectively. The effect of pH adjusted by 0.1 M HCl or NaOH solution was examined in the range of 2–9 with 50 mL of 20 mg L<sup>-1</sup> F<sup>-</sup> solution. 10–50 mg L<sup>-1</sup> of Ca<sup>2+</sup>, Mg<sup>2+</sup>, NO<sub>3</sub><sup>-</sup>, Cl<sup>-</sup>, CO<sub>3</sub><sup>2-</sup>, PO<sub>4</sub><sup>3-</sup> and SO<sub>4</sub><sup>2-</sup> were selected as interfering ions in adsorption condition (*C*<sub>0</sub> = 10 mg L<sup>-1</sup>, pH = 8, *V* = 50 mL) to identify the selectivity of lanthanum methanoate. The residual F<sup>-</sup> concentrations after adsorption were monitored by F<sup>-</sup>-selective electrode using the standard method,<sup>2,32</sup> and the capture capacity of lanthanum methanoate was computed according to our previous work.<sup>11</sup>

### 2.4. Material characterization

The surface morphology and size of lanthanum methanoate were determined by scanning electron microscopy (VEGA300U, Tescan). The pristine and used lanthanum methanoate were verified by X-ray diffraction (D8 ADVANCE, Bruker) equipped with Cu Kα radiation in the 2θ range of 10–80° at 2° min<sup>-1</sup>. XPS measurements were examined using a Thermo Scientific K-Alpha spectrometer (Thermo Fisher, USA). A Nicolet 330 FTIR spectrometer (Thermo Fisher Scientific Ltd, USA) was used to record the Fourier transform infrared spectra (FTIR).

## 3. Results and discussion

### 3.1. Adsorbent characterization

The surface morphology of La-based adsorbent is depicted in Fig. 1a. Clearly, it exhibits a strong polyhedron solid structure and aggregates in block with several small debris on the surface. The particle size of La-based adsorbent is micron with strong solid structure. Fig. 1b displays the EDX mapping of La-based adsorbent, the EDS spectrum indicates that the presence of C, O and La in the particles (Fig. 1c). The structure of the La-based adsorbent was verified by PXRD pattern and FTIR spectra (Fig. 1d and e). The La-based adsorbent possesses sharp and strong characteristic peaks at 2θ = 16.8, 23.8, 29.1, 33.8, 41.6, 44.9, 48.4, 51.5, 54.4, 57.3, 60.0, 62.8, 65.4, 68.1, 70.4, 73.0, 75.6 and 77.9°, which is corresponded to La(COOH)<sub>3</sub> (JCPDS card No. 00-018-0674) reported in the literature<sup>31,33,34</sup> (Fig. 1d), suggesting that the La-based adsorbent is pure La(HCOO)<sub>3</sub>. In the spectrum of La-based adsorbent (Fig. 1e), the band occurred at 3429 cm<sup>-1</sup> corresponds to the –OH stretching vibration. The significant peaks appeared at 1600 cm<sup>-1</sup> and 1426 cm<sup>-1</sup> are

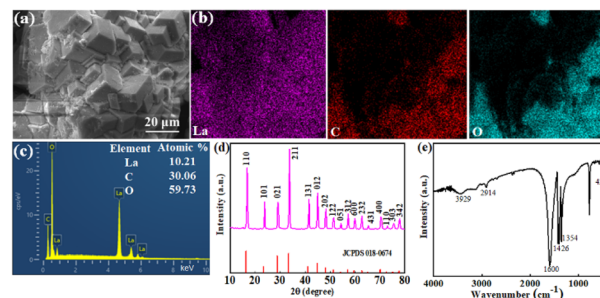


Fig. 1 SEM micrograph (a), EDX elemental mapping (b), EDX analysis (c), PXRD (d) and FT-IR spectrum (e) of La-based adsorbent.



Scheme 1 The diagram of the preparation of La-based adsorbent.



indicative of C–O asymmetric and symmetric vibrations, revealing the carboxylic groups in the methanoate.<sup>33</sup> The bands at 2914  $\text{cm}^{-1}$  and 1354  $\text{cm}^{-1}$  ascribed to the –CH stretching and bending mode illustrates the presence of methanoate,<sup>31</sup> manifesting that the  $\text{La}^{3+}$  ions are successfully coordinated with the groups of –OOCH to generate the  $\text{La}(\text{COOH})_3$ . The peak located at 423  $\text{cm}^{-1}$  represents the La–O stretching vibration in  $\text{La}(\text{COOH})_3$ .<sup>33,34</sup> The  $\text{La}(\text{COOH})_3$  may be generated *via* basic amide-hydrolysis mechanism and the possible pathway is illustrated in Scheme S1† in ESI.<sup>35,36</sup>

## 3.2. Effects of parameters on defluoridation performance

### 3.2.1. Impact of the initial pH values on defluoridation.

The change of pH value can not only affect the charge on the  $\text{La}(\text{COOH})_3$  surface but also affects the existence species of fluoride in the solution. Fig. 2a illustrates the influence of pH on defluoridation of  $\text{La}(\text{COOH})_3$ . It is clear that  $\text{La}(\text{COOH})_3$  exhibits an outstanding defluoridation efficiency over a very broad pH range of 2 to 9, the decontamination performance is more than 85  $\text{mg g}^{-1}$  with original  $\text{F}^-$  concentration of 20  $\text{mg L}^{-1}$  in this pH range. The highest uptake of fluoride is 98.2  $\text{mg g}^{-1}$  at pH of 8. Even at pH of 9, the capture capacity of fluoride is 96.4  $\text{mg g}^{-1}$ . The removal efficiency (85.2  $\text{mg g}^{-1}$ ) is relatively low at pH of 2, since part of  $\text{F}^-$  exist as HF at pH of 2.<sup>1,37</sup> The isoelectric point ( $\text{pH}_{\text{pzc}}$ ) of  $\text{La}(\text{COOH})_3$  assessed using pH drift method<sup>38</sup> is noted as 5.6 (Fig. 2b), implying that the superficies of  $\text{La}(\text{COOH})_3$  is positively charged when  $\text{pH} < 5.6$  which is favourable for defluoridation, and negatively charged when  $\text{pH} > 5.6$ . Hence, the fluoride capture capacity maintains at a relative high level in the pH ranging from 3 to 6 because of the electrostatic attraction between the negative charged  $\text{F}^-$  and the positively charged  $\text{La}(\text{COOH})_3$ .  $\text{La}(\text{COOH})_3$  is deprotonated when  $\text{pH} > \text{pH}_{\text{pzc}}$ . However, with further increase of pH (7–9), the fluoride capture capacity is higher than 96  $\text{mg g}^{-1}$  and reaches the highest value at pH 8, reflecting that the defluoridation of  $\text{La}(\text{COOH})_3$  takes place not only by electrostatic attraction, but also through ligand exchange mechanism between the  $\text{F}^-$  and the –OOCH group of  $\text{La}(\text{COOH})_3$  adsorbent as well as non-specific electrostatic attraction<sup>3,37</sup> at alkaline medium. Hence, a pH of 8 is selected as the optimum pH for subsequent experiments.

**3.2.2. Impact of original  $\text{F}^-$  concentration.** Fig. 3 presents the impact of original  $\text{F}^-$  concentration in the range of 10 to 80

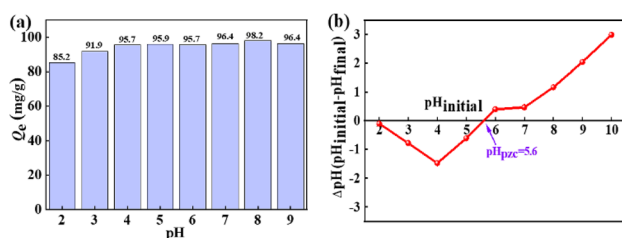


Fig. 2 The impact of pH on defluoridation (a) and  $\text{pH}_{\text{pzc}}$  (b) of the adsorbent.

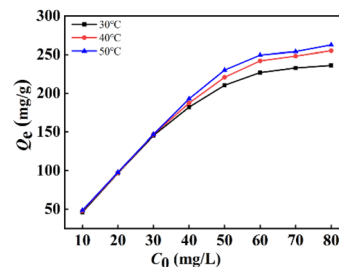


Fig. 3 Impact of original  $\text{F}^-$  concentration on defluoridation by  $\text{La}(\text{COOH})_3$ .

$\text{mg L}^{-1}$  keeping adsorbent dosage fixed at 0.01 g on the defluoridation of  $\text{La}(\text{COOH})_3$  at altered temperature for 12 h. Notably, the  $\text{F}^-$  capture capacity enlarges gradually with the rise of original  $\text{F}^-$  concentration range of 10 to 60  $\text{mg L}^{-1}$  owing to the acceleration of the diffusion rate of  $\text{F}^-$  caused by concentration gradient, and then no significant variation in binding capacity is observed due to the equilibration of binding sites of the  $\text{La}(\text{COOH})_3$  at higher-fluoride solutions under a constant dosage condition. Additionally, at a high fluoride concentration system, the defluoridation process of  $\text{La}(\text{COOH})_3$  is favourable at higher temperature.

**3.2.3. Impact of interfering ions.** To evaluate different interfering ions efficiencies on the defluoridation process in the complex wastewater,  $\text{Ca}^{2+}$ ,  $\text{Mg}^{2+}$ ,  $\text{NO}_3^-$ ,  $\text{Cl}^-$ ,  $\text{CO}_3^{2-}$ ,  $\text{PO}_4^{3-}$  and  $\text{SO}_4^{2-}$  with different initial concentrations were poured into fluoride solution to form 50 mL of binary solutions containing 10  $\text{mg L}^{-1}$  of  $\text{F}^-$  and various interfering ions concentrations (10–50  $\text{mg L}^{-1}$ ), respectively. Clearly, the presence of interfering ions like  $\text{Ca}^{2+}$ ,  $\text{Mg}^{2+}$ ,  $\text{NO}_3^-$ ,  $\text{Cl}^-$ , and  $\text{SO}_4^{2-}$  has little variety in defluoridation performance of  $\text{La}(\text{COOH})_3$  (Fig. 4). Whereas  $\text{PO}_4^{3-}$  and  $\text{CO}_3^{2-}$  exhibit significant interference since the  $\text{p}K_{\text{sp}}$  of  $\text{La}(\text{PO}_4)_3$  and  $\text{p}K_{\text{sp}}$  of  $\text{La}_2(\text{CO}_3)_3$  are 26.16 and 33.4,<sup>39,40</sup> respectively, which are higher than that of  $\text{LaF}_3$  (18.5). The higher the concentration of  $\text{PO}_4^{3-}$  and  $\text{CO}_3^{2-}$  is, the greater interference intensity is. The binding capacities for  $\text{F}^-$  descend from 45.4 to 20.2  $\text{mg g}^{-1}$  and 40.1 to 31.7  $\text{mg g}^{-1}$  as the concentrations of  $\text{PO}_4^{3-}$  and  $\text{CO}_3^{2-}$  increase from 10 to 50  $\text{mg L}^{-1}$ , respectively. Taking all the above-mentioned factors into account, it can be concluded that  $\text{La}(\text{COOH})_3$  prepared in this study has

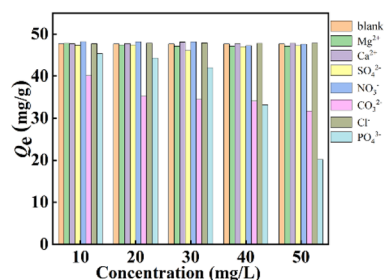


Fig. 4 Effect of interfering ions on the defluoridation performance of  $\text{La}(\text{COOH})_3$ .



a significant anti-interference ability and the inhibitory effect of  $\text{PO}_4^{3-}$  and  $\text{CO}_3^{2-}$  should be particularly concerned in practical complex engineering application.

### 3.2.4. Impact of contact time and adsorption kinetics.

Fig. 5a depicts the time-dependent defluoridation on  $\text{La}(\text{COOH})_3$  under the fixed adsorbent dose of 0.1 g and 1 L of  $\text{F}^-$  solution with various original  $\text{F}^-$  concentrations (10 and 20  $\text{mg L}^{-1}$ ) at pH of 8, respectively. As seen from Fig. 5a, the binding capacity rises rapidly as time increases within 30 minutes, and then attains equilibrium at a contact time of 100 minutes. To interpret the rate-limiting step and determine the defluoridation behaviour of  $\text{La}(\text{COOH})_3$ , three commonly used reaction-based models<sup>41</sup> were conducted to fit the experimentally measured data. The fitting patterns and dependable factors are recorded in Fig. 5b–d and Table 1. Notably, the pseudo-second-order model (PSO) with higher fitted determination coefficients (*i.e.*, 0.9999 at 10  $\text{mg L}^{-1}$  and 0.9999 at 20  $\text{mg L}^{-1}$ ) provide a better description for the kinetics dates than the pseudo-first-order model (PFO), revealing the strong chemical interaction. Meanwhile, the  $Q_e$  (*i.e.*, 95.15 and 201.21  $\text{mg g}^{-1}$  at 10 and 20  $\text{mg L}^{-1}$ ) of  $\text{La}(\text{COOH})_3$  estimated using PSO are accorded with experimental ones (94.96 and 197.10  $\text{mg g}^{-1}$  at 10 and 20  $\text{mg L}^{-1}$ , respectively). Additionally, the diffusion route of  $\text{F}^-$  in the adsorption system is determined by Weber–Morris diffusion model. As portrayed in Fig. 5d, two-platform stages observed in the intra-particle diffusion model mean that the defluoridation on  $\text{La}(\text{COOH})_3$  is consist of multiple diffusion mechanisms. The initial fast stage takes place within 30 min, the maximum adsorption rates ( $k_{id1}$ ) at 10 and 20  $\text{mg L}^{-1}$   $\text{F}^-$  solutions are 3.4649 and 6.3507  $\text{mg g}^{-1} \text{min}^{-0.5}$  during this period, while the adsorption rates ( $k_{id2}$ ) in the subordinate stage occurred between 30 and 100 minutes decline to 0.0964 and 1.3654  $\text{mg g}^{-1} \text{min}^{-0.5}$ , respectively. Notably, none of the two-stage fitting line segments pass through the origin point, which illustrates that the defluoridation process by  $\text{La}(\text{COOH})_3$  is governed by intra-particle diffusion as well as affected by diverse diffusion mechanisms involving surface adsorption, intra-pore diffusion, and external mass transfer.

**Table 1** The fitted factors of kinetics models for defluoridation on  $\text{La}(\text{COOH})_3$

Model	Parameter	$C_0$ ( $\text{mg L}^{-1}$ )	
		10	20
PFO	$k_1 \times 10^2$ ( $\text{min}^{-1}$ )	1.0320	2.5710
	$Q_e$ ( $\text{mg g}^{-1}$ )	7.09	27.11
	$R^2$	0.4709	0.9268
PSO	$k_2 \times 10^2$ ( $\text{g mg}^{-1} \text{min}^{-1}$ )	1.9108	0.2561
	$Q_e$ ( $\text{mg g}^{-1}$ )	95.15	201.21
	$R^2$	0.9999	0.9999
Weber–Morris	$k_{id1}$ ( $\text{mg g}^{-1} \text{min}^{-0.5}$ )	3.4649	6.3507
	$R^2$	0.9984	0.9992
	$k_{id2}$ ( $\text{mg g}^{-1} \text{min}^{-0.5}$ )	0.0964	1.3654
	$R^2$	0.9443	0.9029

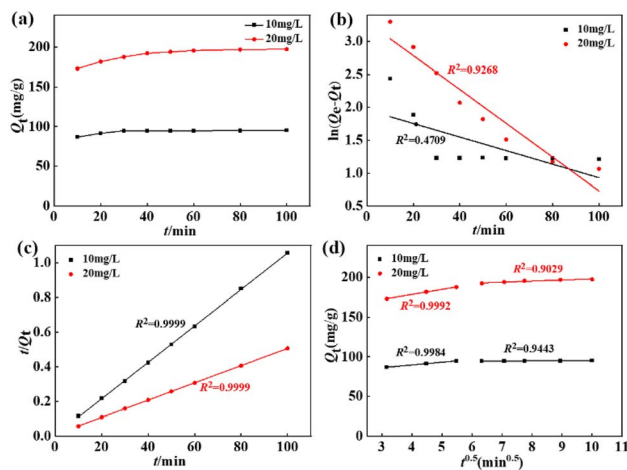


**Fig. 5** Effect of interfering ions on the defluoridation performance of  $\text{La}(\text{COOH})_3$ .

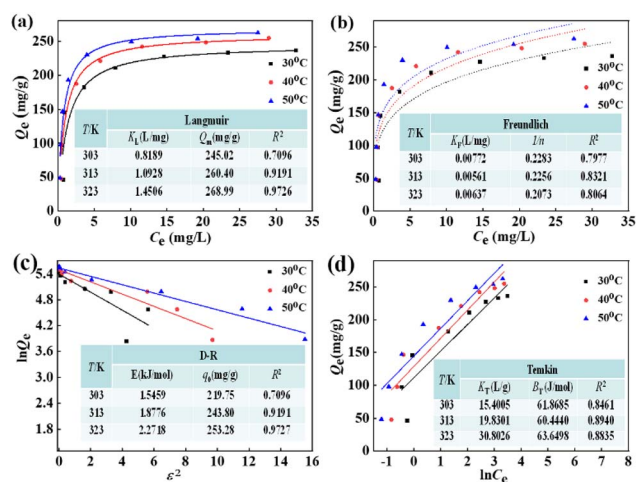


**Fig. 6** Adsorption isotherms of  $\text{F}^-$  on  $\text{La}(\text{COOH})_3$  (a) Langmuir, (b) Freundlich, (c) D–R and (d) Temkin under various temperatures (30–50 °C).

**3.2.5. Adsorption isotherm.** Four classical adsorption isotherms including D–R, Langmuir, Temkin, and Freundlich<sup>42–44</sup> were applied to identify the interactions between the  $\text{F}^-$  equilibrium concentration and binding uptake by  $\text{La}(\text{COOH})_3$  at altered temperature. As displayed in Fig. 6a–d, the corresponding regression coefficients ( $R^2$ ) at temperatures of 30–50 °C are as follows: Langmuir (0.9019, 0.9367 and 0.9644) > Temkin (0.8461, 0.8940 and 0.8835) > Freundlich (0.7977, 0.8321 and 0.8064) > D–R (0.6908, 0.7685 and 0.7753), signifying that the single-layer and homogeneous adsorbed on  $\text{La}(\text{COOH})_3$  dominates the process of defluoridation on the adsorbent. The maximum uptakes for Langmuir models are 245.02, 260.04 and 268.99  $\text{mg g}^{-1}$  at 30, 40 and 50 °C, respectively, which are quite close to experimental values. Obviously, they are much higher than those of reported similar adsorbents listed in Table 2. The free energy ( $E$ ) is computed using the D–R model, as depicted in Fig. 6c. From the calculations, the  $E$  values of  $\text{La}(\text{COOH})_3$  for



Table 2 Comparison of defluoridation capacity for La(COOH)<sub>3</sub> and other studied adsorbents

Adsorbents	pH	C <sub>0</sub> (mg L <sup>-1</sup> )	T/°C	Q <sub>m</sub> (mg g <sup>-1</sup> )	Ref.
HAp-La based MOF	6	8–14	30	4.25	46
La-BDC	5	10–100	25	171.7	3
Ce-TDC MOF	3–9	5–100	25	94.9	45
Al-BTC MOFs	3–10	5–50	25	31.69	48
La@Fu MOF	7	8–14	30	4.75	43
Zirconium based MOFs	3–9	50–700	30	204.08	1
Lanthanide-based MOFs	3–7	—	25	103.95	49
MOF-801	—	8–256	100	166.11	50
MCH-La	3–11	0–80	25	136.78	51
La <sub>2</sub> O <sub>3</sub> -CeO <sub>2</sub> -Fe <sub>3</sub> O <sub>4</sub>	2–10	10–60	25	216.45	52
Bx-Ce-La@500	1–13	10–50	25	88.13	53
Fe-Mg-La	7	10–300	35	47.20	30
La(COOH) <sub>3</sub>	2–9	10–80	30	245.02	This study
			40	260.04	
			50	268.99	

fluoride adsorption are 13.3492, 13.8554 and 14.6897 kJ mol<sup>-1</sup> at 30–50 °C, respectively. It is evident that the values of  $E$  from 8 to 16 kJ mol<sup>-1</sup> manifest that both ligand exchange and electrostatic attraction are the mainly mechanism.<sup>3,43,45–47</sup> To portray the affinity between the F<sup>-</sup> and the La(COOH)<sub>3</sub>, the dimensionless constant separation factor ( $R_L$ ) values calculated according to the literature<sup>21,37</sup> decline quickly with the increasing of initial F<sup>-</sup> concentrations in the range of 10–80 mg L<sup>-1</sup> and approach to zero, manifesting that the adsorbing system is encouraged at even higher F<sup>-</sup> concentrations (Fig. S1†). In addition, the values of  $R_L$  drop as temperature rises and are less than 1. Hence, the defluoridation process of La(COOH)<sub>3</sub> occurs under favorable condition.

**3.2.6. Thermodynamics studies.** To explore the effect of temperature on the defluoridation of La(COOH)<sub>3</sub>, the thermodynamic investigation is utilized to study the defluoridation process (Fig. S2† and Table 3). The calculated  $\Delta H^0$  (41.41 kJ mol<sup>-1</sup>) and  $\Delta S^0$  (166.28 J mol<sup>-1</sup> K<sup>-1</sup>) indicate that the fluoride removal onto La(COOH)<sub>3</sub> is an endothermic nature and random state, revealing that the increase of temperature promotes the capture of fluoride.  $\Delta G^0$  values are -10.26, -12.24 and -13.66 kJ mol<sup>-1</sup> at 30–50 °C, respectively, demonstrating that the defluoridation process on La(COOH)<sub>3</sub> is highly feasible and spontaneous. In addition, the defluoridation mechanism can be further elucidated by thermodynamic factors. The calculated  $\Delta H^0$  (41.41 kJ mol<sup>-1</sup>) is larger than physical adsorption (2.1–20.9 kJ mol<sup>-1</sup>), but less than predicted chemical adsorption (80–400 kJ mol<sup>-1</sup>), implying that the defluoridation on La(COOH)<sub>3</sub> is composed of chemisorption and physisorption process.

Table 3 Thermodynamic factors of defluoridation on La(COOH)<sub>3</sub>

T (°C)	$\Delta G^0$ (kJ mol <sup>-1</sup> )	ln K <sub>D</sub>	$\Delta H^0$ (kJ mol <sup>-1</sup> )	$\Delta S^0$ (J mol <sup>-1</sup> K <sup>-1</sup> )
30	-10.26	58.63	41.41	166.28
40	-12.24	110.30		
50	-13.66	162.86		

### 3.3. Adsorption mechanism via PXRD and XPS characterization

To gain deeper insight into the mechanism of defluoridation by La(COOH)<sub>3</sub>, PXRD and XPS analysis is recorded to verify the changes in structure of pristine and used adsorbent. After fluoride uptake, the characteristic peaks belonged to La(COOH)<sub>3</sub> disappear and a series of new reflections corresponded to the hexagonal phase of LaF<sub>3</sub> (PDF No. 32-0483) emerge in the PXRD pattern<sup>52,54</sup> (Fig. 7a), signifying that precipitation and ligand exchange is identified as the dominating defluoridation mechanism.

Furthermore, XPS analysis is conducted to further elucidate the structural composition of the fresh and used adsorbent. As depicted in Fig. 7b, obvious signals of C and La can be found in the survey spectrum of fresh La(COOH)<sub>3</sub>. As for La 3d, two peaks appeared at 835.3 and 838.4 eV are corresponded to La 3d<sub>5/2</sub>

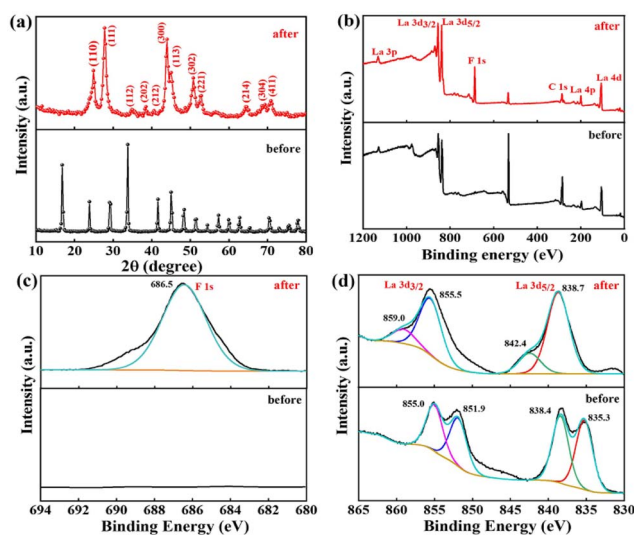
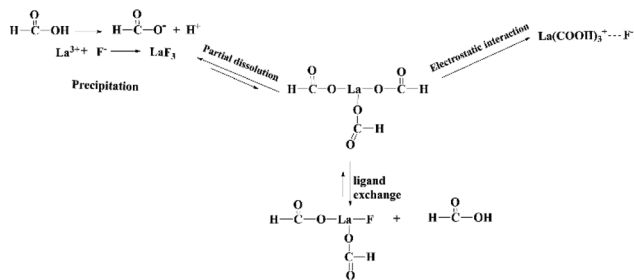


Fig. 7 The used La(COOH)<sub>3</sub> PXRD patterns (a), the fresh and used La(COOH)<sub>3</sub> XPS analysis: (b) survey spectra, (c) F 1s and (d) La 3d of La(COOH)<sub>3</sub>.



Scheme 2 Possible mechanism of defluoridation using  $\text{La(COOH)}_3$ .

spin state, while peaks located at 851.9 and 855.0 eV are ascribed to La  $3d_{3/2}$  orbital.<sup>31,55</sup> After defluoridation, a new F 1s peak centred at 686.5 eV with a slight shift ( $\sim 1.8$  eV) to high binding energy compared with the F 1s standard spectrum of NaF (684.7 eV) emerges in the spectrum,<sup>56,57</sup> revealing that fluoride binding to the  $\text{La(COOH)}_3$  (Fig. 7c). Meanwhile, the La  $3d_{5/2}$  peaks detected at 838.7 and 842.4 eV, and La  $3d_{3/2}$  peaks appeared at 855.5 and 859.0 eV shift to high binding energy direction (3.4–4.0 eV), is attributed to the bond of La–F formed *via* ion exchange as well as precipitation<sup>3</sup> (Fig. 7d). Hence, according to the isoelectric point ( $\text{pH}_{\text{pzc}}$ ) of  $\text{La(COOH)}_3$ , PXRD and XPS analysis, the defluoridation process onto  $\text{La(COOH)}_3$  is significantly controlled by precipitation, ligand exchange between La and fluoride along with the electrostatic interaction, which is in agreement with the previous results obtained from kinetic and isotherm analysis. The possible defluoridation mechanism is shown in Scheme 2.

## 4. Conclusions

Lanthanum methanoate with particle size in micrometre was successfully fabricated for abating excess  $\text{F}^-$  from aqueous solution.  $\text{La(COOH)}_3$  functioned excellently over a wide pH variety from 2 to 9, with the largest decontamination performance at pH of 8. Fluoride adsorption behaviour on  $\text{La(COOH)}_3$  conform with the PSO model and Langmuir isotherm well, reflecting that single-layer chemisorption. The maximum uptakes of  $\text{La(COOH)}_3$  for fluoride achieve 245.02–268.99  $\text{mg g}^{-1}$  at the temperatures of 30–50 °C, respectively, which are better than those of most adsorbents based on rare earth metal elements recorded in the literature. The defluoridation mechanism of  $\text{La(COOH)}_3$  is presided by precipitation, ligand exchange as well as electrostatic attraction. The results illustrate that the synthesized La-based adsorbent can be developed to immobilize fluoride-rich water.

## Author contributions

Conceptualization, investigation, writing – original draft preparation, Weisen Yang, Fengshuo Shi and Shaoju Jian; analysis, Wenlong Jiang; data curation, Yuhuang Chen; methodology, Kaiyin Zhang; writing – review & editing, Shaohua Jiang and Chunmei Zhang; project administration and supervision,

Jiapeng Hu. All authors have read and agreed to the published version of the manuscript.

## Conflicts of interest

There are no conflicts to declare.

## Acknowledgements

The work is financially supported by National Natural Science Foundation of China (51903123); Natural Science Foundation of Fujian Province (No. 2020J01419, No. 2020J01393 and No. 2020J05220); Natural Science Foundation of Jiangsu Province (BK20190760); Central Special Project for Fujian Local Science and Technology Development (No. 2019L3021); National College Students' innovation and entrepreneurship training program (202210397016); The Open Fund of Fujian Provincial Key Laboratory of Green Chemical Technology (WYKF-GCT2021-1).

## References

- 1 L. Zhu, C. Zhang, L. Wang and J. Zhang, *J. Solid State Chem.*, 2022, **307**, 122866.
- 2 N. G. Corral-Capulin, A. R. Vilchis-Nestor, E. Gutiérrez-Segura and M. Solache-Ríos, *J. Fluorine Chem.*, 2018, **213**, 42–50.
- 3 C. Yin, Q. Huang, G. Zhu, L. Liu, S. Li, X. Yang and S. Wang, *J. Colloid Interface Sci.*, 2022, **607**, 1762–1775.
- 4 T. J. Robshaw, R. Dawson, K. Bonser and M. D. Ogden, *Chem. Eng. J.*, 2019, **367**, 149–159.
- 5 M. M. Damtie, Y. C. Woo, B. Kim, R. H. Hailemariam, K. D. Park, H. K. Shon, C. Park and J. S. Choi, *J. Environ. Manage.*, 2019, **251**, 109524.
- 6 W. Yang, C. Li, S. Tian, L. Liu and Q. Liao, *Mater. Chem. Phys.*, 2020, **242**, 122499.
- 7 X. Hu, F. Zhu, L. Kong and X. Peng, *J. Hazard. Mater.*, 2021, **403**, 124039.
- 8 Y.-A. Boussouga, B. S. Richards and A. I. Schäfer, *J. Membr. Sci.*, 2021, **617**, 118452.
- 9 T. N. Bitaw, K. Park and D. R. Yang, *Desalination*, 2016, **398**, 265–281.
- 10 N. Kabay, O. Arar, S. Samatya, U. Yuksel and M. Yuksel, *J. Hazard. Mater.*, 2008, **153**, 107–113.
- 11 S. Jian, Y. Cheng, X. Ma, H. Guo, J. Hu, K. Zhang, S. Jiang, W. Yang and G. Duan, *New J. Chem.*, 2022, **46**, 490–497.
- 12 G. Duan, L. Zhao, C. Zhang, L. Chen, Q. Zhang, K. Liu and F. Wang, *Diamond Relat. Mater.*, 2022, **129**, 109339.
- 13 R. Guo, S. Jiang, M. Hu, Y. Zhan, K. Cheng and G. Duan, *Environ. Sci. Pollut. Res.*, 2021, **28**, 30898–30907.
- 14 L. Chen, Y. Sun, J. Wang, C. Ma, S. Peng, X. Cao, L. Yang, C. Ma, G. Duan, Z. Liu, H. Wang, Y. Yuan and N. Wang, *e-Polym.*, 2022, **22**, 468–477.
- 15 S. Liu, Z. Song, X. Jin, R. Mao, T. Zhang and F. Hu, *Mater. Rep.: Energy*, 2022, **2**, 100077.
- 16 X. Chen, C. Wan, R. Yu, L. Meng, D. Wang, W. Chen, T. Duan and L. Li, *J. Hazard. Mater.*, 2021, **411**, 125113.



- 17 S. Xiao, Y. Zhao, S. Jin, Z. He, G. Duan, H. Gu, H. Xu, X. Cao, C. Ma and J. Wu, *e-Polym.*, 2022, **22**, 719–732.
- 18 Y. Sun, R. Liu, S. Wen, J. Wang, L. Chen, B. Yan, S. Peng, C. Ma, X. Cao, C. Ma, G. Duan, H. Wang, S. Shi, Y. Yuan and N. Wang, *ACS Appl. Mater. Interfaces*, 2021, **13**, 21272–21285.
- 19 W.-Z. Gai and Z.-Y. Deng, *Environ. Sci.: Water Res. Technol.*, 2021, **7**, 1362–1386.
- 20 R. Liu, S. Wen, Y. Sun, B. Yan, J. Wang, L. Chen, S. Peng, C. Ma, X. Cao, C. Ma, G. Duan, S. Shi, Y. Yuan and N. Wang, *Chem. Eng. J.*, 2021, **422**, 130060.
- 21 M. Hossien Saghi, B. Chabot, S. Rezanian, M. Sillanpää, A. Akbar Mohammadi, M. Shams and A. Alahabadi, *Sep. Purif. Technol.*, 2021, **270**, 118645.
- 22 M. Almasi, V. Zelenak, R. Gyepes, L. Zauska and S. Bourrelly, *RSC Adv.*, 2020, **10**, 32323–32334.
- 23 J. Wang, Y. Sun, X. Zhao, L. Chen, S. Peng, C. Ma, G. Duan, Z. Liu, H. Wang, Y. Yuan and N. Wang, *e-Polym.*, 2022, **22**, 399–410.
- 24 B. Xu, I. Masood Ul Hasan, L. Peng, J. Liu, N. Xu, M. Fan, N. K. Niazi and J. Qiao, *Mater. Rep.: Energy*, 2022, **2**, 100139.
- 25 C. Wang, X. Liu, J. P. Chen and K. Li, *Sci. Rep.*, 2015, **5**, 16613.
- 26 Y. Yu and J. P. Chen, *J. Mater. Chem. A*, 2014, **2**, 8086.
- 27 D. T. Lim, T. N. Tuyen, D. N. Nhiem, D. H. Duc, P. N. Chuc, N. Q. Bac, D. X. Tung, N. N. Pham, L. T. V. Ha, N. T. T. Tu, V. T. Nguyen, D. Q. Khieu and D. k. Yi, *J. Nanomater.*, 2021, **2021**, 1–13.
- 28 J. Wang, L. Wu, J. Li, D. Tang and G. Zhang, *J. Alloys Compd.*, 2018, **753**, 422–432.
- 29 M. Govarthan, C. H. Jeon and W. Kim, *Environ. Pollut.*, 2022, **303**, 119049.
- 30 P. Chen, T. Wang, Y. Xiao, E. Tian, W. Wang, Y. Zhao, L. Tian, H. Jiang and X. Luo, *J. Alloys Compd.*, 2018, **738**, 118–129.
- 31 S. M. Prabhu, S. Imamura and K. Sasaki, *ACS Sustainable Chem. Eng.*, 2019, **7**, 6917–6928.
- 32 D. Tang and G. Zhang, *Chem. Eng. J.*, 2016, **283**, 721–729.
- 33 J. Xu, Y. Cui, R. Wang, Z. Shi, C. Wu and D. Li, *Colloids Surf., A*, 2021, **624**, 126689.
- 34 K. Pandi, S. M. Prabhu and J. Choi, *Chemosphere*, 2021, **262**, 127596.
- 35 C. O'Connor, *Q. Rev., Chem. Soc.*, 1970, **24**, 553–564.
- 36 M. Mousavi-Kamazani, S. Alizadeh, F. Ansari and M. Salavati-Niasari, *J. Rare Earths*, 2015, **33**, 425–431.
- 37 S. K. T. Thathsara, P. Cooray, T. K. Mudiyansele, N. Kottegoda and D. R. Ratnaweera, *J. Environ. Manage.*, 2018, **207**, 387–395.
- 38 X. Ma, S. Zhao, Z. Tian, G. Duan, H. Pan, Y. Yue, S. Li, S. Jian, W. Yang, K. Liu, S. He and S. Jiang, *Chem. Eng. J.*, 2022, **446**, 136851.
- 39 S. Shan, Z. Chen, K. Yuen Koh, F. Cui and J. Paul Chen, *J. Colloid Interface Sci.*, 2022, **624**, 691–703.
- 40 X. Zhang, F. Sun, J. He, H. Xu, F. Cui and W. Wang, *Chem. Eng. J.*, 2017, **326**, 1086–1094.
- 41 S. Jiang, M. Zhou, W. Deng, H. Dai, G. Fang and W. Wu, *J. For. Eng.*, 2020, **5**, 101–107.
- 42 Y. Gao, Y. Zhou, Z. Lin, S. Zhang and W. Gao, *J. For. Eng.*, 2021, **6**, 87–93.
- 43 A. Jeyaseelan, M. Naushad and N. Viswanathan, *J. Chem. Eng. Data*, 2020, **65**, 2990–3001.
- 44 Z. Wang, C. Hu, D. Tu, W. Zhang and L. Guan, *J. For. Eng.*, 2020, **5**, 96–102.
- 45 Q. Huang, L. Zhao, G. Zhu, D. Chen, X. Ma, X. Yang and S. Wang, *Sep. Purif. Technol.*, 2022, **298**, 121567.
- 46 A. Jeyaseelan, I. Aswin Kumar, N. Viswanathan and M. Naushad, *J. Colloid Interface Sci.*, 2022, **622**, 228–238.
- 47 Y. Zhang, Y. Qian, W. Li, X. Gao and B. Pan, *Sci. Total Environ.*, 2019, **683**, 609–616.
- 48 N. Zhang, X. Yang, X. Yu, Y. Jia, J. Wang, L. Kong, Z. Jin, B. Sun, T. Luo and J. Liu, *Chem. Eng. J.*, 2014, **252**, 220–229.
- 49 A. Ma, F. Kei, J. Jiang, Q. Yuan, Z. Luo, J. Liu and A. Kumar, *CrystEngComm*, 2017, **19**, 2172.
- 50 F. Ke, C. Peng, T. Zhang, M. Zhang, C. Zhou, H. Cai, J. Zhu and X. Wan, *Sci. Rep.*, 2018, **8**, 939.
- 51 S. Dong and Y. Wang, *Water Res.*, 2016, **88**, 852–860.
- 52 S. Jian, F. Shi, R. Hu, Y. Liu, Y. Chen, W. Jiang, X. Yuan, J. Hu, K. Zhang, S. Jiang, W. Yang and G. Duan, *Compos. Commun.*, 2022, **33**, 101194.
- 53 S. I. Alhassan, H. Wang, Y. He, L. Yan, Y. Jiang, B. Wu, T. Wang, H. Gang, L. Huang, L. Jin and Y. Chen, *J. Hazard. Mater.*, 2022, **430**, 128401.
- 54 H. Khatun, S. S. Mou, A. A. Mortuza and A. Ismail, *Chin. Opt. Lett.*, 2010, **8**, 306–308.
- 55 M. Sengupta, S. Das, S. Bhattacharya, J. Gazi, V. V. D. N. Prasad, S. M. Islam and A. Bordoloi, *Mol. Catal.*, 2022, **522**, 112212.
- 56 M. Gao, W. Wang, M. Cao, H. Yang and Y. Li, *Environ. Res.*, 2020, **188**, 109735.
- 57 C. E. Choong, K. T. Wong, S. B. Jang, I. W. Nah, J. Choi, S. Ibrahim, Y. Yoon and M. Jang, *Chemosphere*, 2020, **239**, 124765.

